Characterizing profile tilt of nanoscale deep-etched gratings via x-ray diffraction

Jungki Song,[1,a)] Ralf K. Heilmann,[1] Alexander R. Bruccoleri,[2] and Mark L. Schattenburg[1]
[1]*Space Nanotechnology Laboratory, MIT Kavli Institute for Astrophysics and Space Research, Massachusetts Institute of Technology, Cambridge, Massachusetts 02139*
[2]*Izentis LLC, PO Box 397002, Cambridge, Massachusetts 02139*

(Received 12 July 2019; accepted 14 October 2019; published 30 October 2019)

The authors report the development of fast, nondestructive, and high accuracy metrology for the characterization of profile tilt relative to the surface normal in nanoscale gratings using x-ray diffraction. Gratings were illuminated with a collimated x-ray beam (Cu K_α), similar to variable-angle small-angle x-ray scattering, to record changes of diffraction efficiency (DE) as a function of incidence angle. Simulations using scalar diffraction theory and rigorous coupled wave analysis predict extrema (0th order DE minimized, ±1st order DE maximized) when local grating bars are parallel to the incident x-ray beam. The surface normal was measured independently by reflecting a laser beam from the grating surface. The independent measurements using x rays and laser beams were referenced to each other via a slit reference plane to characterize the bar tilt angle relative to the surface normal. The fast x-ray measurement can be repeated at arbitrary points to study the spatial variation of the bar tilt angle across large gratings. Two test gratings etched with different deep reactive-ion etch chambers were prepared to investigate the performance of the proposed method. The authors report a repeatability of <0.01° and an accuracy of ~0.08° with a fast scan speed (total integration time of 108 s to scan a line across ~55 mm large grating samples at an interval of ~2 mm). High spatial resolution (<50 μm) can be easily achieved at the expense of speed by limiting the incident x-ray spot size. This process is applicable to any periodic nanostructure as long as x-ray diffraction is well modeled. *Published by the AVS.* https://doi.org/10.1116/1.5119713

I. INTRODUCTION

High aspect ratio etching is a common technique in the semiconductor industry. Bosch deep reactive-ion etching (DRIE) and cryogenic reactive-ion etching are popular techniques for the fabrication of high aspect ratio structures including 3D very large scale integration, through-silicon vias,[1] and x-ray diffractive elements.[2,3] Profile tilt during high aspect ratio etching is a long-known issue, causing overlay errors[4] in IC chip fabrication and reducing diffraction efficiencies (DEs) for x-ray diffractive elements.[3]

Profile tilt is thought to be caused by non-normal bombardment of etch species onto sample surfaces due to a nonuniform plasma sheath.[5] Edge discontinuities in the etch target plane can induce gradients in the plasma sheath near substrate edges to cause "edge tilt."[5] Another possible cause for a nonuniform plasma sheath is positive surface charging of a nonconducting etch mask, which can repel positive etch species to cause a convex profile tilt.[6] Additionally, nonuniform concentration of etch species in the plasma chamber can induce a varying sheath thickness across the sample, resulting in a continuous change of profile tilt angle across the sample.[5] Recent development of a dual-source etch chamber design and installation of a ceramic ring around the sample improved plasma density uniformity to reduce tilt variation.[5]

Previously, destructive and laborious cross-sectional scanning electron microscopy (SEM) imaging was used to characterize profile tilt variations.[5] However, SEM images are easily distorted by aberrations from the electron lens, mechanical drift, and sample charging.[7,8] An exact knife-edge cross-sectional image is required to characterize profile tilt relative to the surface normal with high accuracy. Slow scan speed and sometimes the deposition of a conducting metal layer for imaging can be other drawbacks. Another characterization method uses front and back side alignment of a grid pattern with subsequent deep etching.[5] Profile tilt was measured by analyzing misalignments between the grid mask pattern and the shadow of the deep-etched profile using an optical microscope. However, as it requires a carefully designed test sample, it cannot be used for real-time process monitoring. Overall, the slow, destructive, and unreliable nature of previous measurement techniques limits their applicability for process control of profile tilt in high volume manufacturing.

Characterization of profile tilt is a critical issue in the fabrication of nanoscale critical angle transmission (CAT) gratings in the field of space-based x-ray spectroscopy as well. The CAT grating is a high aspect ratio (200 nm period, ~4–6 μm depth), freestanding silicon grating etched with the Bosch DRIE process.[3] A CAT grating spectrometer, proposed for next generation NASA x-ray telescope missions, requires a large quantity of CAT gratings (~1000) to build high performance scientific instruments.[9,10] The sidewalls of the CAT grating bars should be aligned with high precision (<0.1°, 1σ) relative to incident x rays at a graze angle below the critical angle. This leads to blazing in high diffraction

Note: This paper is part of the Conference Collection: The 63rd International Conference on Electron, Ion, and Photon Beam Technology and Nanofabrication (EIPBN 2019).
[a)]Electronic mail: jksong@mit.edu

orders with high DE.[11] A detailed discussion of the working principle of CAT gratings can be found in Refs. 12 and 13. Since the alignment of CAT gratings using an x-ray beam under vacuum is time-consuming, a laser-based alignment process was developed; however, it must be accompanied with an accurate determination of grating bar tilt relative to the surface normal (called bar-normal angle in this paper).[14,15] Thus, characterizing the bar-normal angle with high accuracy is required.

In this paper, we present a metrology technique to characterize profile tilt of nanoscale gratings via x-ray diffraction. Gratings were illuminated with a collimated x-ray beam (Cu K_α, wavelength = 1.5406 Å), similar to variable-angle small-angle x-ray scattering (SAXS),[16,17] to record the change of DE as a function of the incident angle. Simulations via scalar diffraction theory and rigorous coupled wave analysis (RCWA) predict extrema (0th order DE minimized, ±1st order DE maximized) when local grating bars are parallel to the incident x-ray beam. Since x rays alone cannot characterize the bar-normal angle due to their low reflectivity at near-normal incidence, the surface normal was measured independently by reflecting a laser beam off the grating surface. A special rigid grating mount with slit reference axis was designed to reference the two separate measurements. Thick test gratings with minimal distortion were prepared to investigate the performance of the proposed metrology. We report a bar-normal angle measurement repeatability of <0.01° (1σ) and an accuracy of ~0.08° at a fast scan speed (total integration time of 108 s to scan a line across an ~55 mm large grating at an interval of ~2 mm). The proposed metrology was used to characterize bar-normal angles of CAT gratings and compare with previous synchrotron measurements, with the results showing good agreement.

We believe that the proposed method can be applicable to characterize profile tilt of other periodic nanostructures with appropriate x-ray diffraction modeling. The long penetration depth of x rays is ideal to characterize profile tilt of nanoscale features even on relatively thick substrates. We believe that the fast, nondestructive, and highly sensitive nature of this method makes it a metrology candidate for process monitoring.[18]

II. TEST GRATING SAMPLE PREPARATION

Two test gratings were prepared to study the performance of the proposed metrology. Both were patterned with the same etch mask but etched with different deep reactive-ion etch tools (single source plasma "Pegasus" tool and dual-source plasma "Rapier" tool[5]). Figures 1(a) and 1(b) show

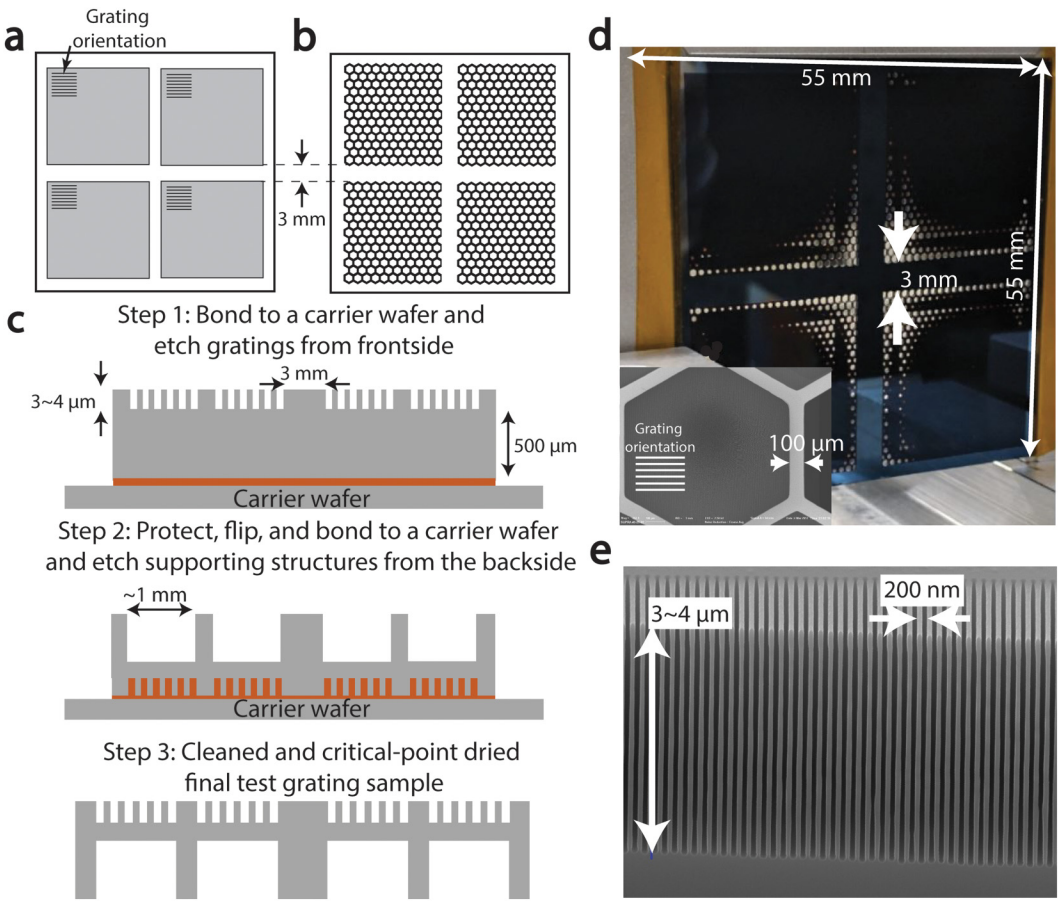

FIG. 1. (a) Design of the front side etch mask. Gray area is filled with 200-nm period grating bars and 5-μm cross-supports running perpendicular to the grating (both the gratings and cross-supports are too small to see). (b) Design of the back side etch mask (not to scale). (c) Fabrication process for the test grating samples (schematic not to scale). (d) Fabricated test gratings. The inset shows an SEM image of a single hexagonal support structure. The gratings are oriented horizontally on the page. (e) Cross-sectional SEM image of 200-nm grating bars etched 3–4 μm deep from the front side.

the etch masks for front and back sides of a bulk silicon wafer. They consist of four rectangular grating patches, 26 × 27 mm in size, patterned on an ~55 mm square chip with 3 mm gaps between patches. The design of each patch is identical to that of recent CAT gratings,[19] comprised of a large array of 1-mm pitch, 100-μm wide hexagonal structural supports on the back side, and 200-nm period grating bars mechanically supported by 5 μm-period cross-supports on the front side. Figure 1(c) shows the fabrication process of the test gratings. 300 nm of oxide was patterned on the front side of bulk silicon wafers and diced to a size of ~55 × 55 mm. Then, the chips were bonded to 100 mm (Pegasus) or 150 mm (Rapier) carrier wafers [step 1, Fig. 1(a)], and the grating bars were deep reactive-ion etched to a depth of 3–4 μm with the Pegasus and Rapier tools. Next, the grating front side was filled with Protek-SR, and the chip was flipped and bonded to 100 mm carrier wafers for back side etching on a Pegasus etcher [step 2, Fig. 1(a)]. The back side pattern was aligned to the front mask and etched until the bulk silicon under the grating bars became thin enough (less than the x-ray absorption length or around 70 μm) to enable observation of transmitted diffraction orders from x-ray illumination. Final test gratings show the bars etched in the front side and hexagonal arrays etched from the back side [step 3, Fig. 1(a)]. Figure 1(d) is a photograph of a test grating sample. The center region near the gap between grating patches was inadvertently over etched due to nonuniform etch rates during DRIE. The inset in Fig. 1(d) is a top view image of the 1-mm pitch, 100-μm hexagonal mesh with the grating bars running horizontally on the page (not resolved). Figure 1(e) shows an inclined SEM image of the grating bars from a cleaved test grating.

III. X-RAY DIFFRACTION

While CAT gratings can be approximated as amplitude gratings in parts of the soft x-ray regime,[12,13] it is reasonably modeled as a "phase grating" in the hard x-ray region (Cu K_α, 8.04 keV) due to its long penetration depth in silicon. Following the discussion in Ref. 20, the relative DEs of CAT gratings can be approximated by the Fourier transform of the complex scalar field modulation. The same scalar theory was used to obtain analytical expressions for absolute DEs of x-ray transmission gratings in the HETGS instrument of the Chandra x-ray telescope.[21,22] Here, we used a numerical approach, including the Radon transform[23] and discrete Fourier transform (DFT), to calculate DEs. First, a Radon transform was performed to calculate path length modulations, $PL(x')$, for each incidence angle. Next, the complex scalar field modulation was derived using the term $e^{ik\Delta nPL(x')}$, where k is the wavenumber, Δn is the refractive index contrast, and x' is a 1D projected axis at the given incident angle. Then, DEs were calculated from the modulus squared of the DFT of the complex scalar field.

RCWA is a more precise method to predict DEs. It slices the grating into stratified layers and solves Maxwell's equations to calculate the fields within each "slice" while matching the boundary conditions. The transmitted fields and resulting DEs are derived using a transfer matrix method.[24]

Straight bars with the bar direction parallel to the surface normal (see the red grating bars inside top graphs, Fig. 2) and skewed bars with the bar direction skewed by −0.286° relative to the surface normal (see the blue grating bars inside bottom graphs, Fig. 2) were considered as illustrative examples. For the simulation of skewed bars with scalar theory, grating depth was corrected by a factor of 1/cos(−0.286). In RCWA, skewed bars were approximated by slicing the grating bars into ten equal stratified layers (see the blue grating bars in bottom graphs, Fig. 2), shifting the grating bar region laterally in each subsequent layer by 2 nm. Figure 2 shows the modeling results for 0th and +1st order DEs as a function of tilt for straight (red) and skewed (blue) bars based on scalar diffraction theory (dashed line) and RCWA (solid line). Tilt is positive clockwise. DE for −1st order almost perfectly overlaps with +1st order DE, and thus

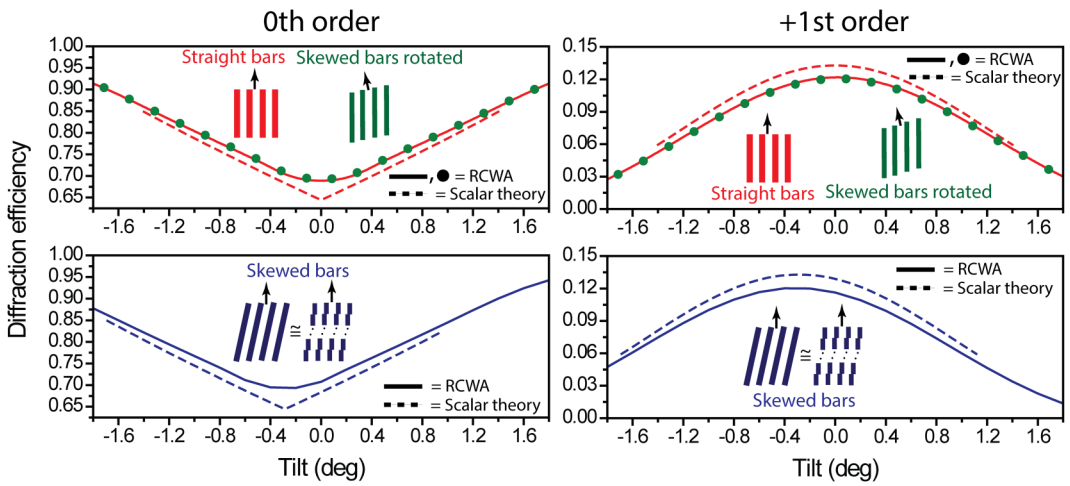

FIG. 2. Prediction of 0th and +1st order DEs for straight bars (red in top graphs), skewed bars (blue in bottom graphs), and skewed bars rotated by skew angle (green in top graphs) as a function of tilt simulated with scalar diffraction theory (dashed line) and RCWA (solid line and circles). Insets inside the graphs are schematic for straight bars, skewed bars, and rotated skewed bars with a black arrow representing the direction of the surface normal. Results for both theories are insensitive to the bar-normal angle.

was not plotted. Regardless of skewed or straight bars, modeling indicates that both 0th and ±1st orders go to extrema (0th order DE minimized, ±1st order DE maximized) when the incident x rays propagate parallel to the grating bars. For straight bars, the surface normal, grating bars, and x rays are all parallel to one another at DE extrema at tilt = 0° (see the red plots in top graphs, Fig. 2). For skewed bars, DEs also reach their extrema when x rays are incident parallel to the bars (at tilt = −0.286°), but with the surface normal inclined by +0.286° (see blue plots in bottom graphs, Fig. 2). Rotating the skewed bars by their skew angle (green) leads to an almost perfect overlap with the results for straight bars (see green circles in top graphs, Fig. 2), demonstrating the sensitivity of our method to measure the angle between the grating bars and x rays, but not the bar-normal angle (i.e., angle between the grating bars and the surface normal).

IV. EXPERIMENT

An x-ray measurement alone is not sufficient to characterize the bar-normal angle as it characterizes only the direction of the grating bars relative to the incident x rays (see Sec. III). Since the surface normal is difficult to measure with x rays at near-normal incidence, a separate measurement using a laser was incorporated. A rigid grating mount equipped with a slit reference plane was designed to correlate two separate measurements performed with x rays and a laser [see Fig. 3(a)]. The grating mount has two slits rigidly aligned ∼100 mm apart from each other using a pair of dowel pins to serve as a reference axis. Surface height variations of the fixed test gratings were measured to be ∼18 μm across the 55 mm square sample, which effectively tilt the grating bar only on the order of ∼0.01° along the scanned lines [see Figs. 3(b) and 3(c)]. Once the grating is mounted, there were no discernible temporal angular drifts during two separate measurements.

Figure 4(a) shows an overview of the experimental procedure. First, the slit reference axis was aligned with a collimated x-ray beam by performing a tilt-scan around the slit reference axis [step 1, Fig. 4(a)]. The inset in step 1 of Fig. 4(a) shows a typical intensity signal during the alignment step. After alignment, the grating mount was translated vertically using a high-precision vertical stage (<10 arc sec of angular error) to allow x rays to be incident on the grating surface. The SAXS system was used to perform SAXS with changing incidence angles (0.4° step, 0.3 s integration time) to find the bar tilt angle relative to the x rays (or relative to the slit reference axis, since the latter was aligned with the x rays in step 1; step 2, Fig. 4). The SAXS system is equipped with a microfocus x-ray source with Cu K_α radiation, Kirkpatrick–Baez type multilayer focusing optics, two pairs of horizontal and vertical slits to control focal spot size, and Pilatus 300 k detector (487 × 719 pixels, 172 μm pitch, 0.0065° angular resolution). Transmitted diffracted orders were imaged on 2D detector arrays located 1.5 m downstream from the sample. Figure 4(b) shows an image of the transmitted diffraction peaks and the corresponding 1D projection onto the grating dispersion axis. Figure 4(c) shows the measured change of DEs for 0th and ±1st orders (points) and the corresponding Lorentzian fits (solid lines). Directions of the grating bars are found by averaging the angles of the extrema in the 0th and 1st order DEs [see the red dotted line in Fig. 4(c)] when the grating bars in the x-ray beam spot are parallel to the incident x rays. After x-ray measurements, the slit reference axis was aligned to a laser beam [step 3, Fig. 4(a)] following the same procedure as shown in step 1 but using a laser. Then, the grating mount was translated vertically so the laser is incident on the grating surface. The direction of the surface normal relative to the laser beam (or to the slit reference axis, since it was aligned to the laser in step 3) was measured using the reflection principle. Steps 1 and 2 together characterize the bar

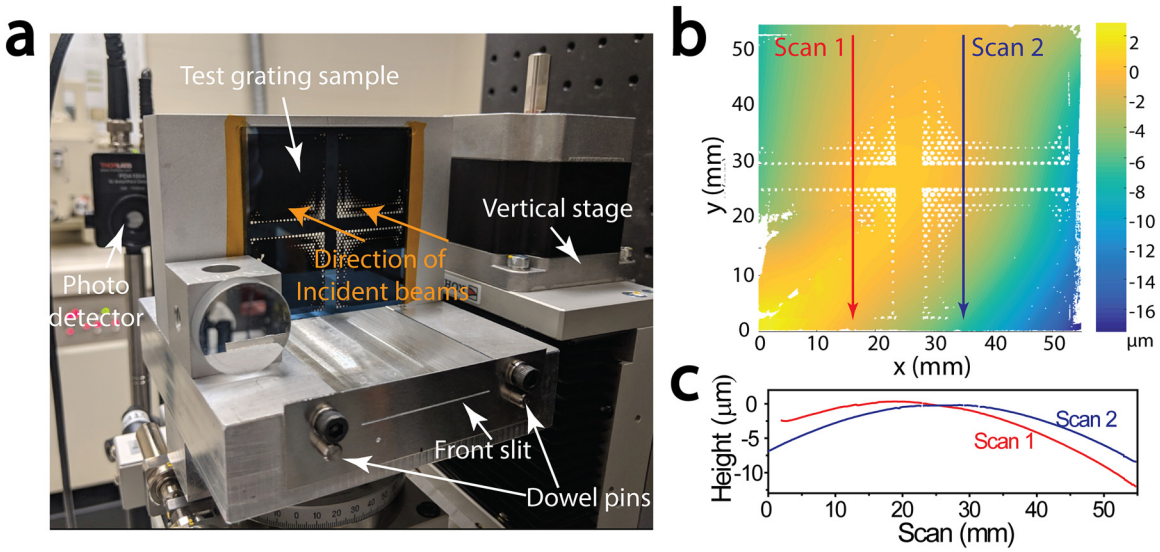

FIG. 3. (a) Test grating fixed in a rigid grating mount. The front slit is rigidly aligned with a back slit (not shown; at the back of the sample). (b) Representative height map of the fixed test grating measured with a Fizeau interferometer. (c) Surface height variations along two line scans.

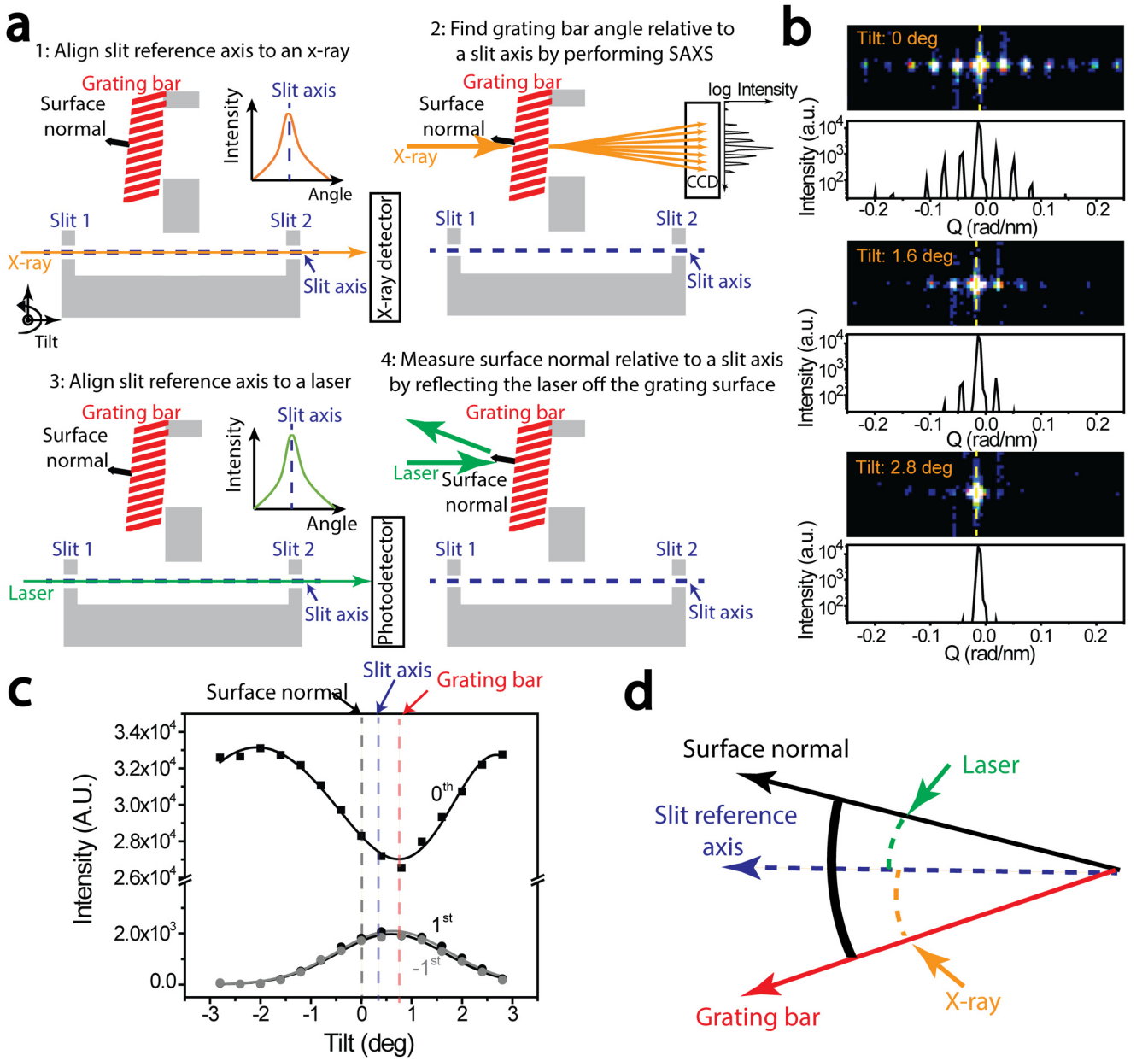

FIG. 4. (a) Experimental procedure. 1: Align the slit reference axis relative to x rays. 2: Measure bar tilt relative to x rays by performing variable-angle SAXS to record the change of DEs. 3: Align slit reference axis relative to the laser. 4: Measure surface normal relative to the laser. (b) 2D image of transmitted diffracted orders with different bar-to-x-ray angles. Each graph shows the spectrum and DEs from −5th to 5th orders. (c) Representative data (points) and Lorentzian fits (lines) from variable-angle SAXS. The surface normal was used as a reference for plotting. (d) Schematic showing arbitrary directions of the surface normal, grating bars, and the slit reference axis (to be aligned parallel to x rays and the laser in steps 1 and 3). The bar-normal angle (black solid angle) is characterized by combining two separate measurements using an x-ray beam (orange dotted angle) and a laser (green dotted angle).

angle relative to the slit reference axis [orange dotted angle in Fig. 4(d)]. Steps 3 and 4 together characterize the surface normal relative to the slit reference axis [green dotted angle in Fig. 4(d)]. Putting it all together, we can characterize the bar-normal angle [black solid angle in Fig. 4(d)].

V. RESULTS AND DISCUSSION

A. Bar tilt measurements on the test grating sample

Bar tilt angle variation in the test grating sample was measured by repeating a variable-angle SAXS (step 2, Fig. 4) along the direction perpendicular to the grating lines. The surface normal was found only once since mechanical distortion of the fixed test grating is negligibly small compared to the etch angle distribution [see Figs. 3(b) and 3(c)]. Figures 5(a) and 5(c) show bar tilt angle variations from two test gratings etched with the Pegasus and Rapier tools. Two line scans were performed [see insets in Figs. 5(a) and 5(b)]. The bar angle is positive counterclockwise relative to the surface normal. Figures 5(b) and 5(d) are graphical representations of bar angle variations for Pegasus- and Rapier-etched gratings, respectively. Dotted lines indicate the relative variation of plasma sheath thickness deduced from the bar tilt angle variations.

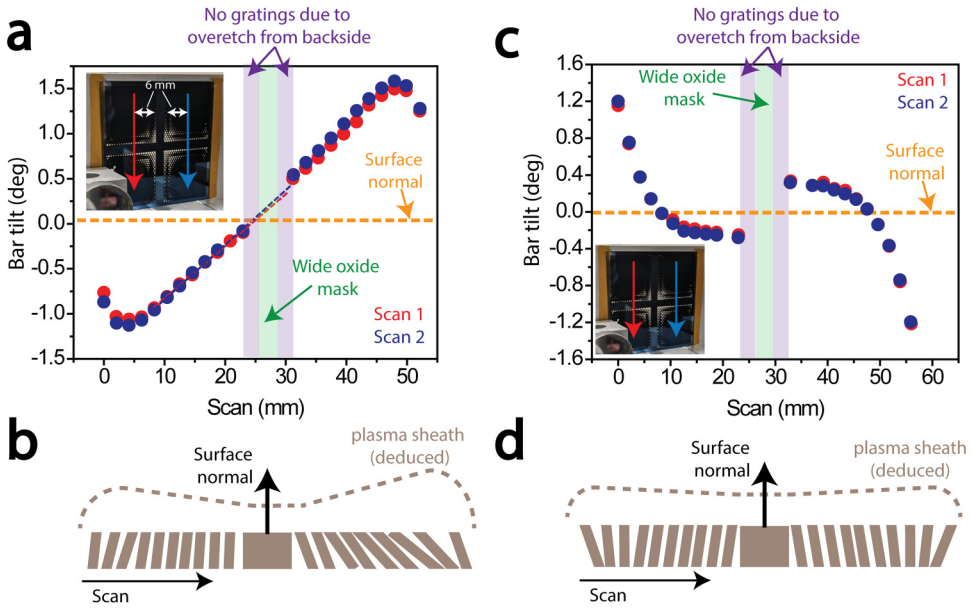

FIG. 5. Bar tilt variations along a line perpendicular to the grating bars for Pegasus- (a) and Rapier-etched (c) gratings. Scans 1 and 2 were performed 6 mm away from chip edges [see insets in (a) and (c)]. Data from top patch were extrapolated (dashed lines) toward the center wide oxide mask for visual help. Surface normals were used as references for plotting. Graphical interpretations of bar tilt variations for Pegasus- (b) and Rapier-etched (d) gratings. Relative plasma sheath thickness is deduced from the spatial variation of the bar tilt angle.

Edge effects are clearly visible near <10 mm from the top and bottom edges of both samples likely due to the nonperpendicular electric field caused by the termination of the plasma sheath. A linear change of the bar tilt angle is visible near the central region (5–47 mm) in the Pegasus-etched gratings [0.6 °/mm, see Fig. 5(a)], while the Rapier-etched gratings [see Fig. 5(c)] show nearly constant bar tilt near the central region (10–25 mm and 33–45 mm). A very similar trend of data was reported by the plasma etcher manufacturer.[5] It was claimed that the more advanced Rapier tool generates a more uniform plasma density, resulting in uniform profile tilt.[5] An asymmetric plasma sheath can be deduced for the Pegasus-etched grating from the asymmetric bar angles around the surface normal in the Pegasus data [Figs. 5(a) and 5(b)], while a symmetric plasma sheath is deduced for the Rapier-etched grating [Figs. 5(c) and 5(d)].[25] A sudden jump of the bar tilt angle is clearly observed in the Rapier sample [Fig. 5(c)] across a wide gap masked with a nonconducting oxide mask. We speculate that positive charging of the nonconducting, wide (~3 mm) oxide etch mask strip repels positive SF_6 ions during the etching steps, causing convex bar angle distributions.[6] A similar phenomenon can be deduced from the Pegasus data [see Fig. 5(a)] since—if we linearly extrapolate the data set from a left data set (scan 6–22 mm)—it does not line up with the data from its right data set (scan 31–46 mm); the right data set is shifted positive relative to extrapolated data from a left data set [see linearly extrapolated lines in Fig. 5(a)]. It is suspected that surface charge from a wide oxide mask contributes to bar angle variations in addition to what is expected from nonuniform plasma density alone.

Repeatability in characterizing the bar-normal angle was measured to be <0.01° (1σ). Accuracy is estimated to be ~0.08°, which is sufficient for the alignment of CAT gratings in a high-efficiency, high-resolving-power x-ray spectrograph.[10,26] Both repeatability and accuracy were derived by the root-sum-square of uncertainties from x-ray and laser measurements. The main factor limiting the accuracy of our measurements is due to yet-to-be-optimized laser measurements (~0.07°), which can be improved with additional effort. The statistical error of x-ray measurements using a high-precision SAXS tool comprises a small portion of the error budget (<0.03°). Nonrectangular and asymmetric grating profile could shift the extrema of 0th and ±1st DEs from the "nominal" grating bar direction and bias the measurement results. However, under the assumption that bar shapes are uniform across the grating, this bias can be corrected in the assembly process by aligning CAT gratings to blaze certain diffraction orders.

High spatial resolution can be easily achieved, at the expense of speed, by simply changing the x-ray spot size with pairs of slits in the SAXS tool. In this work, only 108 s of integration time was required to line scan across ~55 mm test grating samples at an interval of ~2 mm using a 50-μm square x-ray beam.

B. Bar tilt measurements on CAT gratings

The developed metrology technique was applied to characterize variations of bar-normal angle in freestanding CAT gratings. CAT gratings are etched from silicon-on-insulator wafers, where the grating bars are etched into the device layer and the hexagonal mesh is etched into the handle layer, with the buried oxide (BOX) layer serving as a stop for both etches. The BOX layer is subsequently removed from the open areas.[3] More details on the fabrication of CAT gratings can be found in Ref. 3.

Insets in Figs. 6(a) and 6(b) show a square ($32 \times 32\ mm^2$) and a rectangular ($8 \times 32\ mm^2$) CAT grating, respectively. These gratings were etched with the same Pegasus tool, and thus the same trend of linear bar tilt variations is expected. Figure 6(a) shows bar tilt variations (~0.06 °/mm) of the square CAT grating measured from both sides along the same points using the proposed metrology technique. Measurements from both sides show good agreement with each other. Since thin, freestanding CAT gratings can display slight out-of-plane buckling in a freestanding grating within a hexagonal cell[15,27] (curvature of the sample will mechanically tilt the bar angle), there can be subtle discrepancies between front and back side measurements [see Fig. 6(b)] if the measurement positions do not overlap perfectly.

Bar tilt variations of CAT gratings, measured with the proposed metrology technique, agree with observations from synchrotron data. Figure 6(b) is an example synchrotron data set taken at an x-ray wavelength of 2.5 nm for a rectangular CAT grating [see the inset in Fig. 6(b)]. The data show the DEs of diffraction orders 4–6 along a line scan. The illumination angle, relative to the surface normal, was kept constant during the scan such that x rays are incident on the bar sidewalls at a small grazing angle, nominally optimizing diffraction into 5th order. The fast variations in the DEs (about one cycle every 0.87 mm) are due to partial blockage of the $\sim 0.15 \times 0.35\ mm^2$ beam footprint by the hexagonal support grid. The slowly varying envelope is due to a gradual change in the tilt angle of the illuminated grating bars as the sample is translated along the scanned line. The deduced bar tilt angle change as a function of beam footprint position is on the order of 0.05 °/mm and in good agreement with the observation from Pegasus-etched gratings [see Figs. 5(a) and 6(a)].

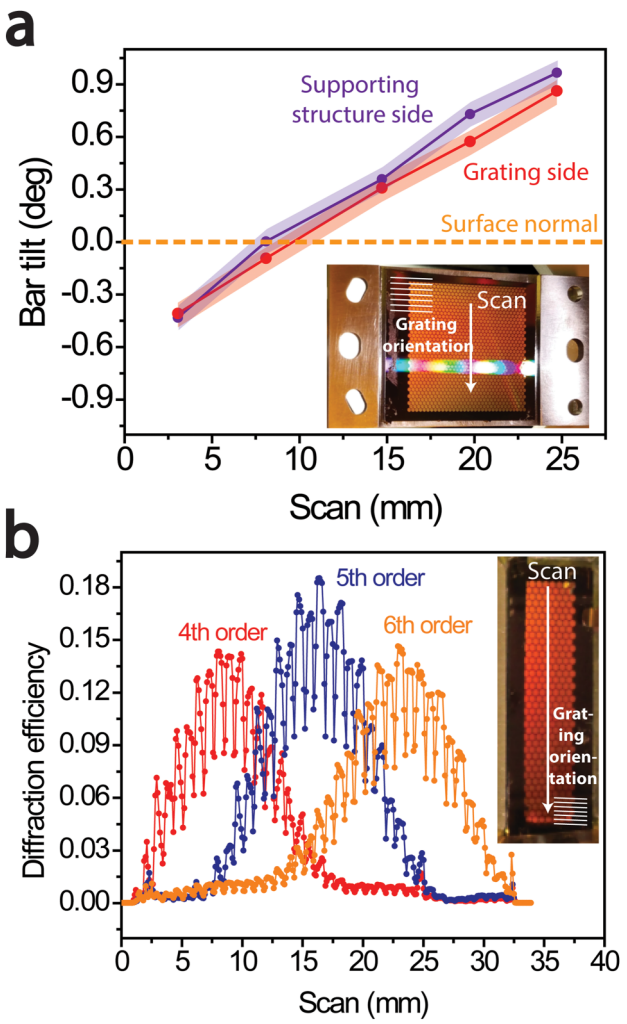

FIG. 6. (a) Bar tilt variations of a square ($32 \times 32\ mm^2$) CAT grating relative to surface normal measured with the proposed metrology technique. Measurements were performed with both grating side (red) and the opposite side (purple) facing the x-ray source. Surface normals were used as references for plotting. Inset shows a square ($32 \times 32\ mm^2$) CAT grating etched with the Pegasus tool and mounted on a titanium frame. (b) Change of DEs of the consecutively blazed orders 4–6 along a scan line measured with an x-ray wavelength of 2.5 nm at a synchrotron facility. Inset shows the measured rectangular ($8 \times 32\ mm^2$) CAT grating etched with the Pegasus tool.

In an actual spectrometer application, a readout camera would cover several diffraction orders at once, which means that every part of the grating will contribute to the effective area of the instrument. However, if the bar tilt variations become too large, photons may end up in orders that miss the readout, or the critical angle may be exceeded, also leading to a loss of effective area. It is, therefore, of interest to keep the profile tilt within a certain range, depending on the specific instrument design and desired grating size. For CAT gratings, only etch angle variations along the grating dispersion direction are important; along the perpendicular direction, observed efficiency variations are insignificant (see, for example, Fig. 3 in Ref. 28).

VI. CONCLUSION AND FUTURE PLANS

We have demonstrated a fast and nondestructive metrology technique to characterize bar-normal angle variations via integrated x-ray and laser measurements. We report a repeatability of <0.01° and an accuracy of ~0.08° with a clear path for further improvements. High spatial resolution (<50 μm square) can readily be achieved at the expense of scan speed. The technique was used to resolve spatial variations of bar-normal angles in test gratings presumed to be caused by edge and mask effects and nonuniform plasma density. Bar angle variations of CAT gratings measured with this method and with a soft x-ray synchrotron beam show good agreement. We believe that this method can be extended to characterize profile tilt in many other periodic nanostructures with appropriate modeling of x-ray diffraction. With longer exposure time, other geometrical parameters such as sidewall angle, depth, and duty cycle can be derived precisely following similar procedures used in the critical dimension SAXS technique. In the future, we hope to characterize other geometrical parameters such as bar shape, duty cycle variations, and thickness variations with more detailed diffraction modeling.[29,30]

ACKNOWLEDGMENTS

The authors acknowledge support from NASA Research Opportunities in Earth and Space Science Strategic Astrophysics

Technology (Grant No. NNX17AG43G). This work made use of the Shared Experimental Facilities at the MIT supported in part by the MRSEC Program of the National Science Foundation under Award No. DMR–1419807. The authors thank C. Settens for technical assistance in using shared x-ray facilities at the MIT. The synchrotron data were taken at beamline 6.3.2 of the Advanced Light Source, which is a Department of Energy (DOE) Office of Science User Facility under Contract No. DE-AC02-05CH11231.

[1]M. M. Shulaker, T. F. Wu, M. M. Sabry, H. Wei, H.-S. Philip Wong, and S. Mitra, *Proceedings of the Design, Automation, and Test in Europe Conference and Exhibition*, Grenoble, France, 9–13 March 2015 (IEEE, 2015) p. 1197.
[2]H. Miao, A. A. Gomella, N. Chedid, L. Chen, and H. Wen, Nano Lett. **14**, 3453 (2014).
[3]A. R. Bruccoleri, R. K. Heilmann, and M. L. Schattenburg, J. Vac. Sci. Technol. B **34**, 06KD02 (2016).
[4]H. Lee *et al.*, Proc. SPIE **10959**, 1095907 (2019).
[5]R. Barnett, D. Thomas, Y. Song, D. Tossell, T. Barrass, and O. Ansell, *2010 Proceedings 60th Electronic Components and Technology Conference (ECTC)*, Las Vegas, NV, 1–4 June 2010 (IEEE, New York, 2010), p. 1056.
[6]S. Murakawa, S. Fang, and J. P. McVittie, Appl. Phys. Lett. **64**, 1558 (1994).
[7]M. T. Postek, A. E. Vladar, and P. Cizmar, Proc. SPIE **9173**, 917306 (2014).
[8]M. T. Postek and A. E. Vladár, Proc. SPIE **9556**, 95560Q (2015).
[9]R. K. Heilmann, J. Kolodziejczak, A. R. Bruccoleri, J. A. Gaskin, and M. L. Schattenburg, Appl. Opt. **58**, 1223 (2019).
[10]H. M. Günther and R. K. Heilmann, J. Astron. Telesc. Instrum. Syst. **5**, 021003 (2019).
[11]R. K. Heilmann *et al.*, Proc. SPIE **10699**, 106996D (2018).
[12]R. K. Heilmann, M. Ahn, E. M. Gullikson, and M. L. Schattenburg, Opt. Express **16**, 8658 (2008).
[13]R. K. Heilmann, M. Ahn, A. Bruccoleri, C.-H. Chang, E. M. Gullikson, P. Mukherjee, and M. L. Schattenburg, Appl. Opt. **50**, 1364 (2011).
[14]J. Song, R. K. Heilmann, A. R. Bruccoleri, M. L. Schatternburg, and E. Hertz, Proc. SPIE **10399**, 1039915 (2017).
[15]J. Song, R. K. Heilmann, A. R. Bruccoleri, E. Hertz, and M. L. Schattenburg, Proc. SPIE **10699**, 106990S (2018).
[16]R. L. Jones *et al.*, Appl. Phys. Lett. **83**, 4059 (2003).
[17]Z. Ma and D. G. Seiler, *Metrology and Diagnostic Techniques for Nanoelectronics* (Pan Stanford, New York, 2017).
[18]N. G. Orji *et al.*, Nat. Electron. **1**, 532 (2018).
[19]R. K. Heilmann *et al.*, Proc. SPIE **10399**, 1039914 (2017).
[20]J. W. Goodman, *Introduction to Fourier Optics* (W. H. Freeman, New York, 2017).
[21]K. F. Fischbach *et al.*, Proc. SPIE **0982**, 273 (1988).
[22]M. L. Schattenburg, C. R. Canizares, D. Dewey, A. M. Levine, T. H. Markert, and H. I. Smith, Proc. SPIE **298**, 210 (1988).
[23]J. S. Lim, *Two-Dimensional Signal and Image Processing* (Prentice-Hall, Englewood Cliffs, NJ, 1990).
[24]M. G. Moharam and T. K. Gaylord, J. Opt. Soc. Am. **71**, 811 (1981).
[25]M. Varvara, R. Barnett, F. Avril, and P. Bennett, *Transducers* (IEEE, Anchorage, AK, 2015), p. 1172.
[26]H. M. Günther, C. T. DeRoo, R. K. Heilmann, E. Hertz, R. K. Smith, and J. Wilms, Proc. SPIE **10699**, 106996F (2018).
[27]R. K. Heilmann, A. R. Bruccoleri, and M. L. Schattenburg, Proc. SPIE **9603**, 960314 (2015).
[28]R. K. Heilmann, A. R. Bruccoleri, J. Kolodziejczak, J. A. Gaskin, S. L. O'Dell, R. Bhatia, and M. L. Schattenburg, Proc. SPIE **9905**, 99051X (2016).
[29]T. Hu *et al.*, J. Appl. Phys. **96**, 1983 (2004).
[30]D. F. Sunday, S. List, J. S. Chawla, and R. J. Kline, J. Appl. Crystallogr. **48**, 1355 (2015).